Dynamically encircling an exceptional point through phase-tracked closed-loop control

Sen Zhang[1], Yangyu Huang[1], Lei Yu[2], Kaixuan He[2], Ning Zhou[2],
Dingbang Xiao[1], Xuezhong Wu[1], Franco Nori[3,4], Hui Jing[5]* & Xin Zhou[1]*

[1]College of Intelligence Science and Technology, NUDT, Changsha, 410073, China.
[2]East China Institute of Photo-Electronic IC, Bengbu, 233042, China.
[3]Center for Quantum Computing (RQC), RIKEN, Wakoshi, Saitama, 351-0198, Japan.
[4]Department of Physics, University of Michigan, Ann Arbor, MI 48109-1040, USA.
[5]Key Laboratory of Low-Dimensional Quantum Structures and Quantum Control
of Ministry of Education, Hunan Normal University, Changsha, 410081, China.
*e-mail: jinghui73@foxmail.com; zhouxin11@nudt.edu.cn.

CONTENTS

SUPPLEMENTARY NOTE 1. DEVICE FABRICATION

As illustrated in Supplementary Fig. 7a, the fabrication of the device commences with a 6-inch silicon-on-insulator (SOI) wafer. This wafer comprises a 10 µm-thick P-type ⟨100⟩ single-crystal silicon conductive layer with a resistivity of 0.01 Ω·cm, a 3 µm-thick oxide layer, and a 500 µm-thick single-crystal silicon handle layer. The fabrication process involves several key steps:

1. Platform etching: Shallow cavities are etched into the conductive layer of the substrate SOI using a deep reactive ion etching (DRIE) technique to create bonding platforms and conductive routings. Importantly, the tops of the bonding platforms remain unetched, while the tops of the conductive routings are etched, achieving a height of 5 µm. Prior to this etching process, alignment marks are etched on the handle layer to facilitate subsequent patterning and bonding operations.

2. Wafer direct bonding: A structure SOI is then bonded to the etched substrate SOI through a direct wafer bonding process. This structure SOI consists of a 100 µm-thick P-type ⟨100⟩ single-crystal silicon structural layer, also exhibiting a resistivity of 0.01 Ω·cm, in addition to a 3 µm-thick oxide layer and a 450 µm-thick single-crystal silicon handle layer. The structure layer of the second SOI is tightly bonded to the platforms of the substrate SOI.

3. Chemical mechanical polishing (CMP): The handle and oxide layers of the structure SOI are subsequently removed using a CMP process, leaving a 100 µm-thick structural layer firmly bonded to the substrate SOI.

4. Metal pads patterning: With the aid of the previously etched alignment marks, metal pads are patterned and spurted onto the structural layer to facilitate wire bonding.

5. Structure release: The structure layer is patterned using a photolithography process and then etched through using a DRIE process to release the resonator, the electrodes, and the pads. The alignment of the structure with the platforms underneath is guaranteed using the alignment marks.

The completed wafer, as depicted in Supplementary Fig. 7b, contains a total of 333 devices. The dicing process employs stealth laser cutting along the dicing lanes shown in Supplementary Fig. 7c, during which the laser is focused inside the wafer to induce a series of defects. These internal imperfections serve as starting points for crack propagation. By applying tension to the tape adhered to the wafer's underside, the devices are separated from the cut lanes due to stress concentration. This technique avoids contamination of the bare devices, as the laser cutting occurs internally. Finally, the microscopic image of a fabricated non-Hermitian MEMS resonator is presented in Supplementary Fig. 7d, and the device is subsequently packaged in a carrier to maintain a vacuum of 0.001 Pa, thereby substantially mitigates air damping effects.

SUPPLEMENTARY NOTE 2. EQUATIONS OF MOTION AND THE EFFECTIVE HAMILTONIAN

A. Equations of motion in driving frames

We commence with the classical Newtonian equations of motion for the system, described by

$$\begin{bmatrix} \ddot{x} \\ \ddot{y} \end{bmatrix} + \begin{bmatrix} \gamma_1 & 0 \\ 0 & \gamma_2 \end{bmatrix} \begin{bmatrix} \dot{x} \\ \dot{y} \end{bmatrix} + \begin{bmatrix} \omega_1^2 + \Delta_\mathrm{p}/2 & \Delta_\mathrm{p}/2 \\ \Delta_\mathrm{p}/2 & \omega_2^2 + \Delta_\mathrm{p}/2 \end{bmatrix} \begin{bmatrix} x \\ y \end{bmatrix} = \begin{bmatrix} F\cos(\omega_\mathrm{d} t)/m \\ 0 \end{bmatrix}, \tag{S.1}$$

where $\Delta_\mathrm{p} = 2\kappa V_0 V_\mathrm{p} \cos(\omega_\mathrm{p} t) - 2\kappa V_\mathrm{p}^2/2$. We apply the rotating-wave approximation that considers higher-harmonic idler waves, the displacements can be expanded as

$$\begin{aligned} x &= \sum_{m=-\infty}^{\infty} \frac{1}{2} A_m e^{-i(\omega_\mathrm{d}+m\omega_\mathrm{p})t} + \text{c.c.}, \\ y &= \sum_{m=-\infty}^{\infty} \frac{1}{2} B_m e^{-i(\omega_\mathrm{d}+m\omega_\mathrm{p})t} + \text{c.c.}, \end{aligned} \tag{S.2}$$

where c.c. denotes complex conjugation, A_m and B_m are the slowly varying complex amplitudes of the m-th idler wave. The 0-th idler wave is the exact mode itself. Substituting (S.2) into (S.1) and omitting the second-order time derivatives of the complex amplitudes, we have,

$$\begin{aligned} &\left[\gamma_1 - 2i(\omega_\mathrm{d} + m\omega_\mathrm{p})\right] \dot{A}_m - \left[(\omega_\mathrm{d} + m\omega_\mathrm{p})^2 - \omega_1^2 + \frac{\kappa V_\mathrm{p}^2}{4} + i\gamma_1(\omega_\mathrm{d} + m\omega_\mathrm{p})\right] A_m \\ &-\frac{\kappa V_\mathrm{p}^2}{4} B_m + \frac{\kappa V_0 V_\mathrm{p}}{2}(A_{m-1} + A_{m+1}) + \frac{\kappa V_0 V_\mathrm{p}}{2}(B_{m-1} + B_{m+1}) = \frac{F}{2m}\delta_{m,0}, \end{aligned} \tag{S.3}$$

$$\begin{aligned} &\left[\gamma_2 - 2i(\omega_\mathrm{d} + m\omega_\mathrm{p})\right] \dot{B}_m - \left[(\omega_\mathrm{d} + m\omega_\mathrm{p})^2 - \omega_2^2 + \frac{\kappa V_\mathrm{p}^2}{4} + i\gamma_2(\omega_\mathrm{d} + m\omega_\mathrm{p})\right] B_m \\ &-\frac{\kappa V_\mathrm{p}^2}{4} A_m + \frac{\kappa V_0 V_\mathrm{p}}{2}(B_{m-1} + B_{m+1}) + \frac{\kappa V_0 V_\mathrm{p}}{2}(A_{m-1} + A_{m+1}) = 0. \end{aligned} \tag{S.4}$$

In this study, actuation is applied to mode 1, $\omega_\mathrm{d} \sim \omega_1$. The pump frequency is tuned close to the frequency difference, $\omega_\mathrm{p} \sim \Delta\omega \equiv \omega_2 - \omega_1$. Consequently, this configuration facilitates the up-conversion of the drive and pump, which effectively reaches mode 2, $\omega_\mathrm{d} + \omega_\mathrm{p} \sim \omega_2$. To simplify our analysis, we focus exclusively on the first-order dynamical interaction, which is captured by setting $m = 0$ in (S.3) and $m = 1$ in (S.4),

$$(\gamma_1 - 2i\omega_\mathrm{d})\dot{A}_m - \left(\omega_\mathrm{d}^2 - \omega_1^2 + \frac{\kappa V_\mathrm{p}^2}{4} + i\gamma_1\omega_\mathrm{d}\right) A_0 + \frac{\kappa V_0 V_\mathrm{p}}{2} B_1 = \frac{F}{2m}, \tag{S.5}$$

$$\begin{aligned} &\left[\gamma_2 - 2i(\omega_\mathrm{d} + \omega_\mathrm{p})\right] \dot{B}_1 - \left[(\omega_\mathrm{d} + \omega_\mathrm{p})^2 - \omega_2^2 + \frac{\kappa V_\mathrm{p}^2}{4} + i\gamma_2(\omega_\mathrm{d} + \omega_\mathrm{p})\right] B_1 \\ &+ \frac{\kappa V_0 V_\mathrm{p}}{2} A_0 = 0. \end{aligned} \tag{S.6}$$

By dividing equations (S.5) and (S.6) by $2\omega_1$ and $2\omega_2$, respectively, we derive the approximated first-order equations of motion within the driving rotating frames,

$$i\begin{bmatrix}\dot{A}_0\\ \dot{B}_1\end{bmatrix}=\begin{bmatrix}\omega_1-\frac{\kappa V_\mathrm{p}^2}{8\omega_1}-\omega_\mathrm{d}-i\gamma_1/2 & \frac{\kappa V_0 V_\mathrm{p}}{4\omega_1}\\ \frac{\kappa V_0 V_\mathrm{p}}{4\omega_2} & \omega_2-\frac{\kappa V_\mathrm{p}^2}{8\omega_2}-\omega_\mathrm{p}-\omega_\mathrm{d}-i\gamma_2/2\end{bmatrix}\begin{bmatrix}A_0\\ B_1\end{bmatrix}-\begin{bmatrix}\frac{F}{4m\omega_1}\\ 0\end{bmatrix}.$$

During the calculations, we employ several approximations: $\gamma_{1,2}/(2\omega_{1,2})\sim 0$, $\omega_\mathrm{d}\sim\omega_1$, $\omega_\mathrm{d}+\omega_\mathrm{p}\sim\omega_2$, $(\omega_\mathrm{d}^2-\omega_1^2)/(2\omega_1)\sim\omega_\mathrm{d}-\omega_1$, and $[(\omega_\mathrm{d}+\omega_\mathrm{p})^2-\omega_2^2]/(2\omega_2)\sim\omega_\mathrm{d}+\omega_\mathrm{p}-\omega_2$. Updating B_1 by a slightly scaled variable $B_1\omega_2/\omega_1$, we can further obtain the formal first-order equations of motion for the system in the driving frames,

$$i\begin{bmatrix}\dot{A}_0\\ \dot{B}_1\end{bmatrix}=\begin{bmatrix}\Omega_1-\omega_\mathrm{d}-i\gamma_1/2 & g\\ g & \Omega_2-\omega_\mathrm{d}-i\gamma_2/2\end{bmatrix}\begin{bmatrix}A_0\\ B_1\end{bmatrix}-\begin{bmatrix}f\\ 0\end{bmatrix}, \tag{S.7}$$

where, $\Omega_1=\omega_1-\kappa V_\mathrm{p}^2/(8\omega_1)$, $\Omega_2=\omega_2-\kappa V_\mathrm{p}^2/(8\omega_2)-\omega_\mathrm{p}$, $g=\kappa V_0 V_\mathrm{p}/(4\omega_1)$, and $f=F/(4m\omega_1)$.

B. Effective Hamiltonian

The equations of motion (S.7) are formulated in fast rotating driving frames of ω_d for mode 1 and $\omega_\mathrm{d}+\omega_\mathrm{p}$ for mode 2. To facilitate analysis, we now transform these equations into a slowly rotating frame of ω_p, which is known as the Floquet frame. This transformation is achieved by letting

$$\begin{aligned}x_0&=\frac{1}{2}A_0e^{-i\omega_\mathrm{d}t}+\text{c.c.},\\ y_1&=\frac{1}{2}B_1e^{-i\omega_\mathrm{d}t}+\text{c.c.},\end{aligned}$$

or

$$\begin{aligned}A_0&=2x_0e^{i\omega_\mathrm{d}t}-A_0^*e^{2i\omega_\mathrm{d}t},\\ B_1&=2y_1e^{i\omega_\mathrm{d}t}-B_1^*e^{2i\omega_\mathrm{d}t}.\end{aligned} \tag{S.8}$$

where the superscript "*" denotes the complex conjugation of the variable. Substituting (S.8) into (S.7), we have

$$\begin{aligned}&2i(\dot{x}_0+i\omega_\mathrm{d}x_0)e^{i\omega_\mathrm{d}t}-i(\dot{A}_0^*+2i\omega_\mathrm{d}A_0^*)e^{2i\omega_\mathrm{d}t}\\ &=\left(\Omega_1-\omega_\mathrm{d}-i\frac{\gamma_1}{2}\right)\left(2x_0e^{i\omega_\mathrm{d}t}-A_0^*e^{2i\omega_\mathrm{d}t}\right)+g\left(2y_1e^{i\omega_\mathrm{d}t}-B_1^*e^{2i\omega_\mathrm{d}t}\right)\\ &-2f\cos(\omega_\mathrm{d}t)e^{i\omega_\mathrm{d}t}+fe^{2i\omega_\mathrm{d}t},\end{aligned} \tag{S.9}$$

$$\begin{aligned}&2i(\dot{y}_1+i\omega_\mathrm{d}y_1)e^{i\omega_\mathrm{d}t}-i(\dot{B}_1^*+2i\omega_\mathrm{d}B_1^*)e^{2i\omega_\mathrm{d}t}\\ &=\left(\Omega_2-\omega_\mathrm{d}-i\frac{\gamma_2}{2}\right)\left(2y_1e^{i\omega_\mathrm{d}t}-B_1^*e^{2i\omega_\mathrm{d}t}\right)+g\left(2x_0e^{i\omega_\mathrm{d}t}-A_0^*e^{2i\omega_\mathrm{d}t}\right)\end{aligned} \tag{S.10}$$

Equating the coefficients of like power of $e^{i\omega_{\mathrm{d}}t}$ in (S.9) and (S.10), we have

$$
\begin{aligned}
i\dot{x}_0 &= \left(\Omega_1 - i\frac{\gamma_1}{2}\right)x_0 + gy_1 - f\cos(\omega_{\mathrm{d}}t), && \text{(S.11)}\\
i\dot{A}_0^* &= \left(\Omega_1 + \omega_{\mathrm{d}} - i\frac{\gamma_1}{2}\right)A_0^* + gB_1^* - f, && \text{(S.12)}
\end{aligned}
$$

and

$$
\begin{aligned}
i\dot{y}_1 &= \left(\Omega_2 - i\frac{\gamma_2}{2}\right)y_1 + gx_0, && \text{(S.13)}\\
i\dot{B}_1^* &= \left(\Omega_2 + \omega_{\mathrm{d}} - i\frac{\gamma_2}{2}\right)B_1^* + gA_0^*, && \text{(S.14)}
\end{aligned}
$$

Equations (S.12) and (S.14) are the equations of motion in the negative-frequency frames, which are conjugations of (S.7). Equations (S.11) and (S.13) constitute the equations of motion in the Floquet frame,

$$
i\begin{bmatrix}\dot{x}_0\\ \dot{y}_1\end{bmatrix} = \begin{bmatrix}\Omega_1 - i\gamma_1/2 & g\\ g & \Omega_2 - i\gamma_2/2\end{bmatrix}\begin{bmatrix}x_0\\ y_1\end{bmatrix} - \begin{bmatrix}f\cos(\omega_{\mathrm{d}}t)\\ 0\end{bmatrix}. \tag{S.15}
$$

The dynamic matrix of the equations of motion (S.15) is regarded as the effective Hamiltonian,

$$
\mathbf{H} = \begin{bmatrix}\Omega_1 - i\frac{\gamma_1}{2} & g\\ g & \Omega_2 - i\frac{\gamma_2}{2}\end{bmatrix} = \begin{bmatrix}\omega_1 - \frac{\kappa V_{\mathrm{p}}^2}{8\omega_1} - i\frac{\gamma_1}{2} & g\\ g & \omega_1 - \frac{\kappa V_{\mathrm{p}}^2}{8\omega_2} - \delta_{\mathrm{p}} - i\frac{\gamma_2}{2}\end{bmatrix}. \tag{S.16}
$$

where δ_{p} is the detuning of the pump, $\delta_{\mathrm{p}} \equiv \omega_{\mathrm{p}} - \Delta\omega$. The eigenvalues of this non-Hermitian Hamiltonian is obtained by calculating $\det(\mathbf{H} - \lambda\mathbf{I}) = 0$,

$$
\begin{aligned}
\lambda_\pm =& \frac{\Omega_1 + \Omega_2}{2} - i\frac{\gamma_1 + \gamma_2}{4} \pm \sqrt{\left(\frac{\Omega_2 - \Omega_1}{2} - i\frac{\gamma_2 - \gamma_1}{4}\right)^2 + g^2}\\
=& \omega_1 - \frac{\kappa V_{\mathrm{p}}^2}{16}\left(\frac{1}{\omega_1} + \frac{1}{\omega_2}\right) - i\frac{\gamma_1 + \gamma_2}{4}\\
&\pm \sqrt{\left[\frac{\kappa V_{\mathrm{p}}^2}{16}\left(\frac{1}{\omega_1} - \frac{1}{\omega_2}\right) - \frac{\delta_{\mathrm{p}}}{2} - i\frac{\gamma_2 - \gamma_1}{4}\right]^2 + g^2}.
\end{aligned} \tag{S.17}
$$

C. Steady-state responses

The steady-state information of the system can be obtained by letting $\dot{A}_0 = \dot{B}_1 = 0$ for (S.7), which gives

$$
\begin{bmatrix}A_0\\ B_1\end{bmatrix} = \begin{bmatrix}\Omega_1 - \omega_{\mathrm{d}} - i\gamma_1/2 & g\\ g & \Omega_2 - \omega_{\mathrm{d}} - i\gamma_2/2\end{bmatrix}^{-1}\begin{bmatrix}f\\ 0\end{bmatrix}, \tag{S.18}
$$

The complex amplitudes of the mode 1 and the first idler wave of mode 2 are given by

$$A_0 = f\frac{\Omega_2 - \omega_{\rm d} - i\gamma_2/2}{(\omega_{\rm d} - \lambda_+)(\omega_{\rm d} - \lambda_-)}, \tag{S.19}$$

$$B_1 = f\frac{-g}{(\omega_{\rm d} - \lambda_+)(\omega_{\rm d} - \lambda_-)}. \tag{S.20}$$

The theoretical amplitude responses are obtained by calculating $|A_0|$ and $|B_1|$. The phase response of mode 1 is given by $-\mathrm{Arg}(A_0)$. It is noteworthy that the phase of the mode-2 idler wave is not directly represented by $-\mathrm{Arg}(B_1)$ due to the contribution of the pump phase to the overall phase of the idler wave. Since the pump phase is arbitrary and uncontrollable in this study, the overall phase of the mode-2 idler wave is undetectable.

SUPPLEMENTARY FIGURES.

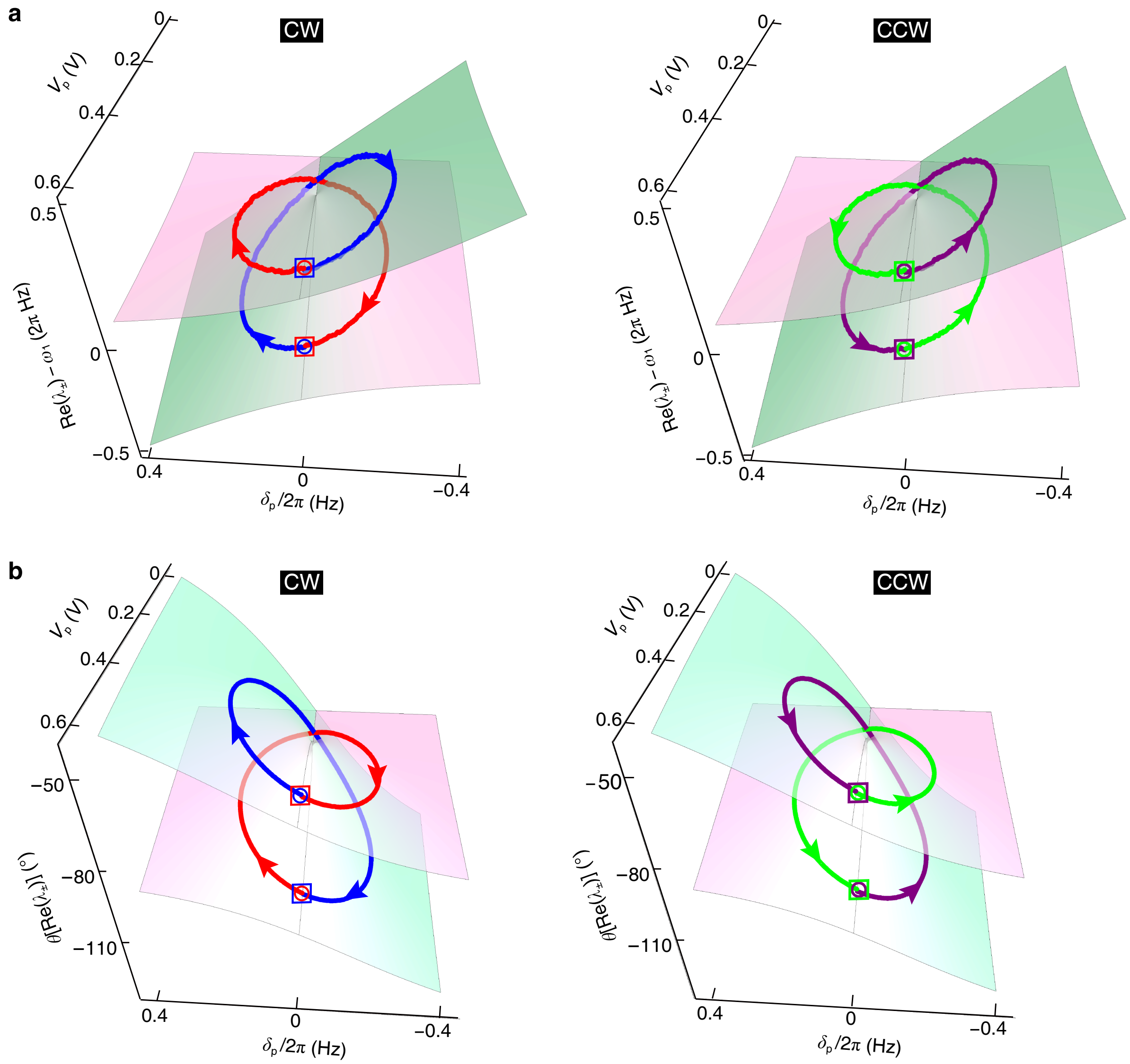

Supplementary Figure 1. **Results of the smoothly encircling of EP with a circular trajectory.** (**a**) The phase-tracked closed-loop oscillation frequencies for the CW encircling process starting from the high-frequency sheet (red curve), the CW encircling process from the low-frequency sheet (blue curve), the CCW encircling process from the high-frequency sheet (purple curve), and the CCW encircling process from the low-frequency sheet (green curve) smoothly evolve on the $\mathrm{Re}(\lambda_\pm)$ Riemann surface. The circles and squares denote the start/end points of the encircling trajectories on the high and low-frequency sheets, respectively. The arrow indicates the direction. (**b**) The corresponding tracked phases for the four encircling processes. The colors on all the surfaces correspond to the imaginary part $\mathrm{Im}(\lambda_\pm)$ of the eigenvalues.

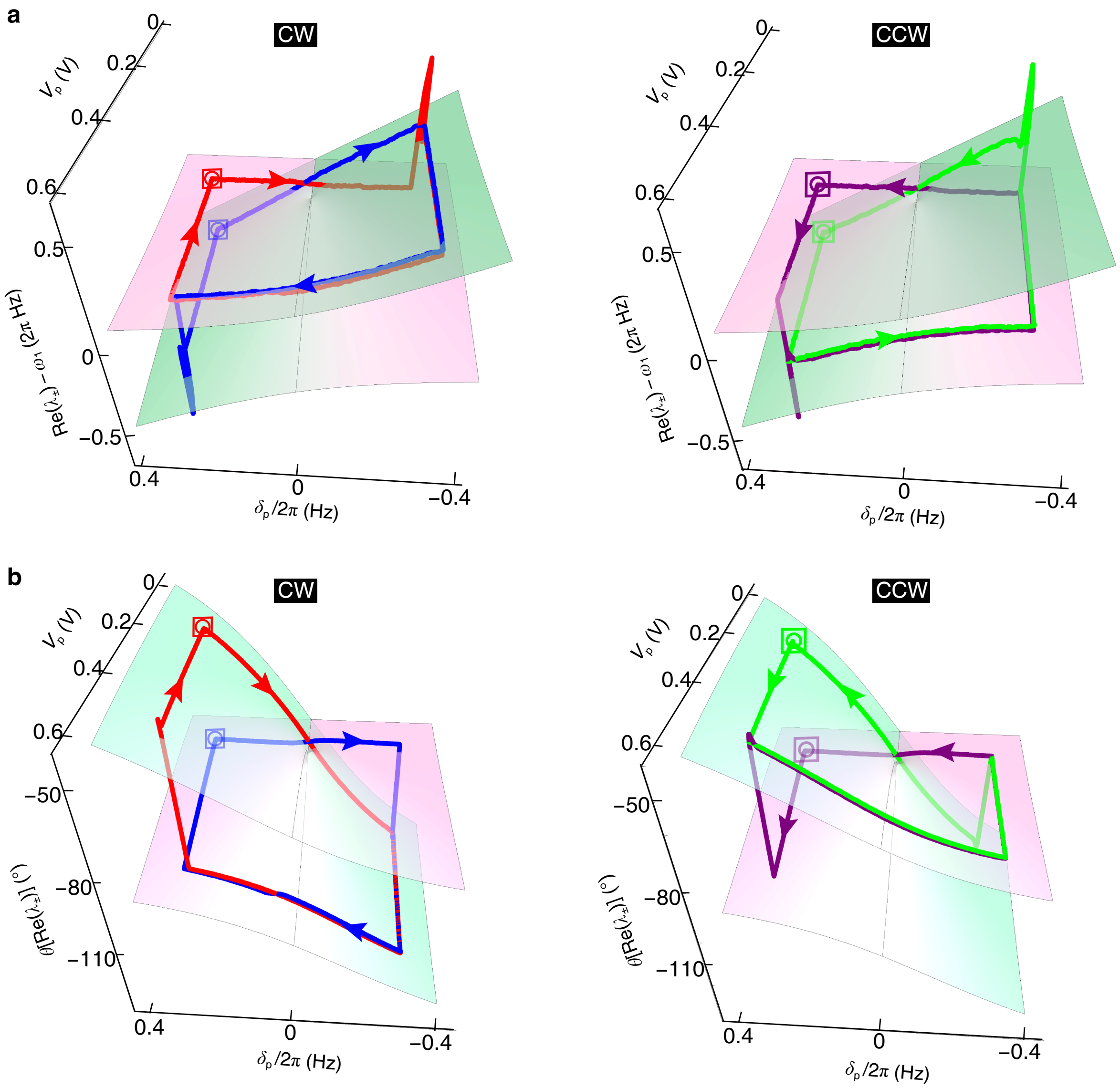

Supplementary Figure 2. **Results of non-adiabatic transitions through phase-tracked closed-loop control.** (**a**) The phase-tracked closed-loop oscillation frequencies for the CW encircling process starting from the high-frequency sheet (red curve), the CW encircling process from the low-frequency sheet (blue curve), the CCW encircling process from the high-frequency sheet (purple curve), and the CCW encircling process from the low-frequency sheet (green curve) exhibit a transition between the high- and low-frequency sheets of the Riemann surface in lower-loss states. The circles and squares denote the start/end points of the encircling trajectories on the high and low-frequency sheets, respectively. The arrow indicates the direction. (**b**) The corresponding tracked phases for the four encircling processes. The colors on all the surfaces represent the system's energy dissipation, with pink indicating low-loss states and cyan representing high-loss states.

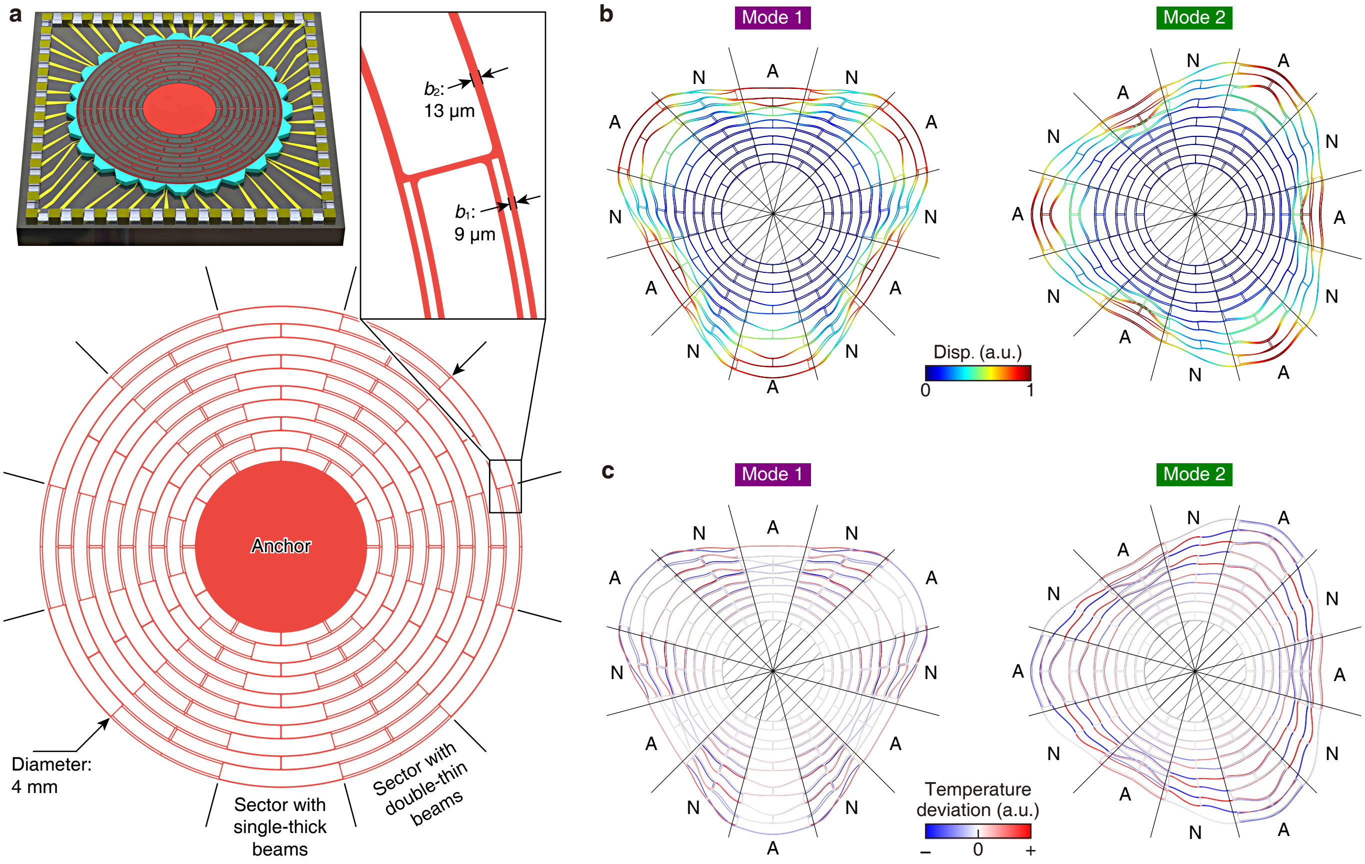

Supplementary Figure 3. **Device Design.** (**a**) Structure of the non-Hermitian disk resonator, highlighted in red. The capacitive electrodes are indicated in cyan, while the electric routings and pads are marked in yellow. The substrate is shown in gray. The resonator has a diameter of 4 mm and a height of 100 μm, with a capacitive gap of 9 μm. The widths of the thin and thick beams are 9 μm and 13 μm, respectively. (**b**) The six-node in-plane standing-wave modes displaying normalized displacements. (**c**) The instantaneous temperature-deviation fields resulting from thermal-elastic coupling.

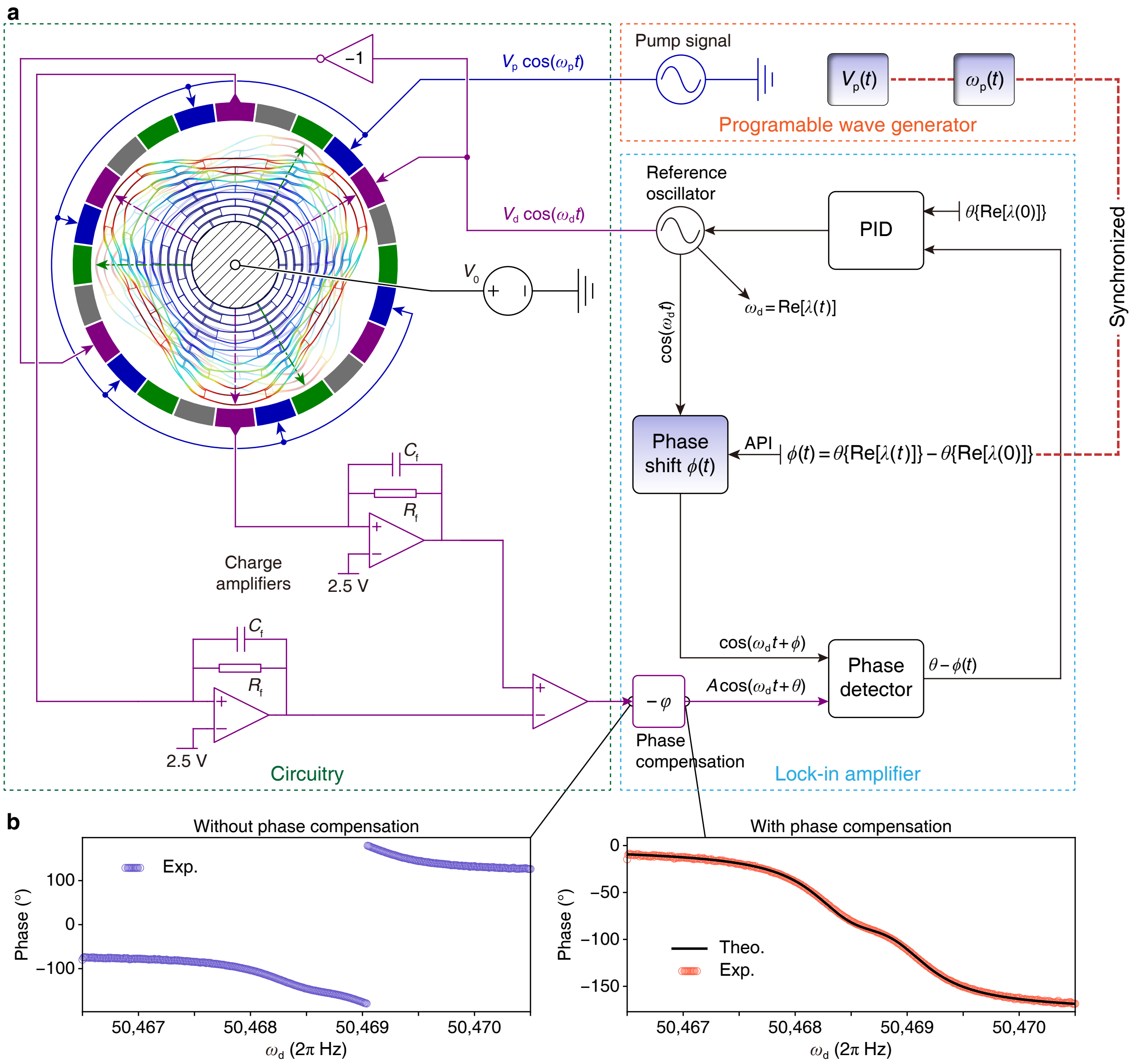

Supplementary Figure 4. **Detailed experimental setup.** (**a**) Mode 1 is actuated differentially, and its response displacement is measured capacitively. A parametric pump with adjustable amplitude and frequency is employed to modulate the coupling stiffness. An adaptive PLL is implemented within a Zurich Instruments MFLI lock-in amplifier to track the phase $\theta\{\mathrm{Re}[\lambda_{\pm}(t)]\}$ in real-time. The wave generator and the lock-in amplifier are synchronized to facilitate the coordinated variations of $V_{\mathrm{p}}(t)$, $\delta_{\mathrm{p}}(t)$, and $\phi(t)$. (**b**) The test circuitry can introduce an additional phase $\varphi = -65^{\circ}$ to the output signal. This phase shift is compensated before the output signal is put into the phase detector. The left and right panels illustrate the phases of the open-loop output signal without and with phase compensation, respectively. The black curve represents the theoretically expected response phase, given by $\theta = -\mathrm{Arg}(\chi_1)$.

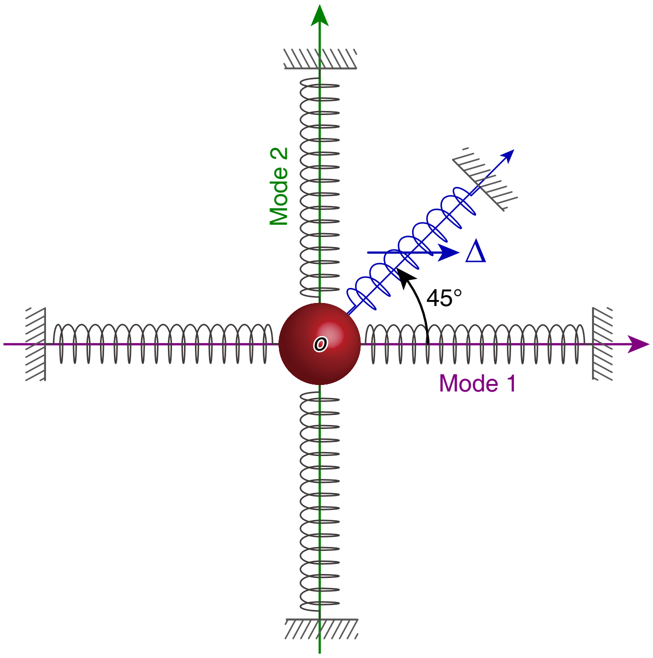

Supplementary Figure 5. **Reduced-order model of the dynamical coupling of the two operational modes.** Modes 1 and 2 can be represented as two orthogonal degrees of freedom of a single proof mass. The parametric pump is equivalent to the Floquet dynamical modulation of a spring oriented at a 45° off-axis angle.

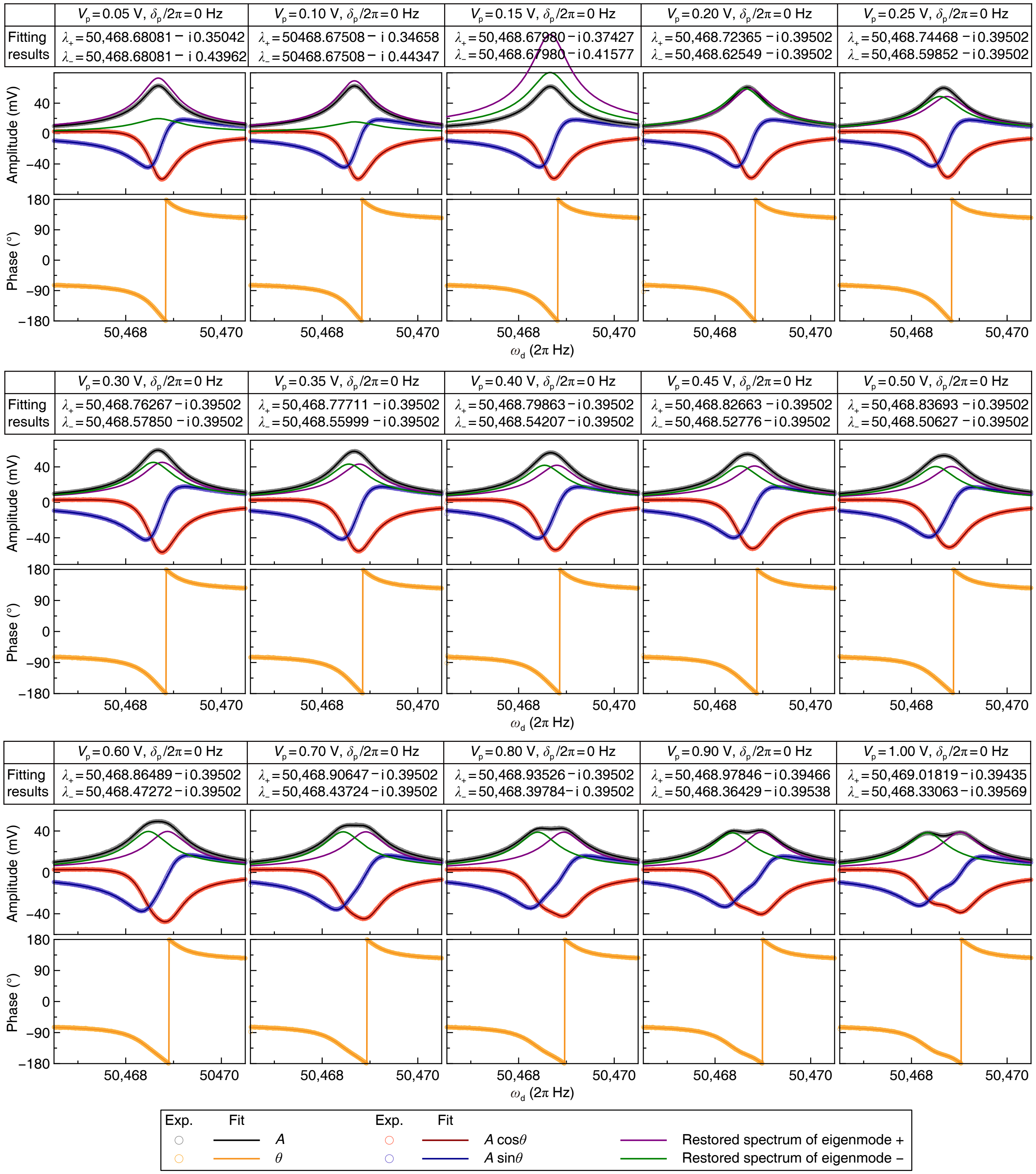

Supplementary Figure 6. **Fitting processes of the frequency responses to obtain the complex eigenvalues.** The in-phase and quadrature components of the measured data are fitted to the real and imaginary parts of the modified susceptibility, respectively, to extract the complex eigenvalues. Exp., experimental results. Fit., fitting results.

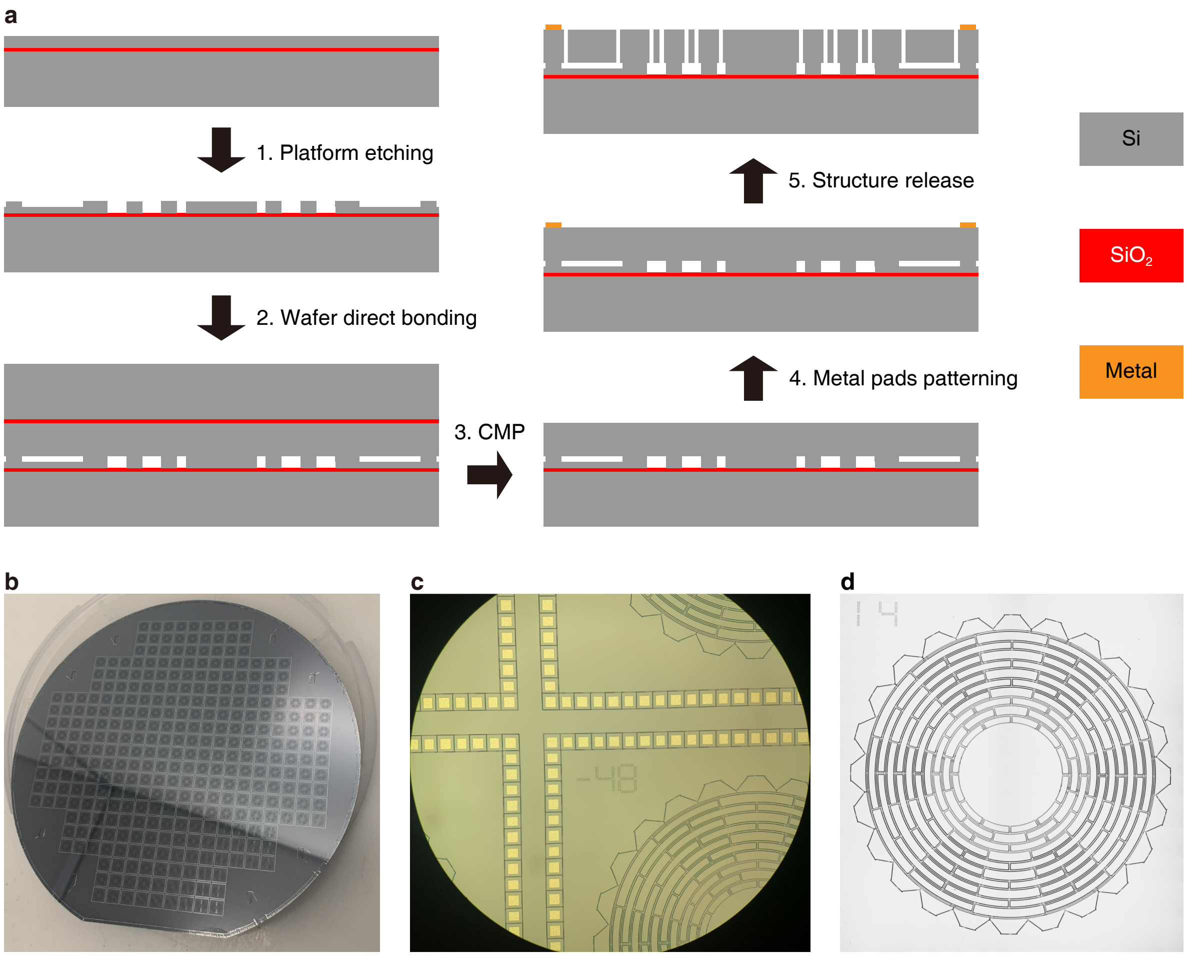

Supplementary Figure 7. **Fabrication of the non-Hermitian MEMS resonator.** (**a**) MEMS fabrication process of the devices. (**b**) The fabricated 6-inch wafer with 333 devices. (**c**) Details of the dicing lanes. (**d**) The microscopic picture of a non-Hermitian MEMS disk resonator.